

PAPER

From soft to hard magnetic Fe–Co–B by spontaneous strain: a combined first principles and thin film study

To cite this article: L Reichel *et al* 2015 *J. Phys.: Condens. Matter* **27** 476002

View the [article online](#) for updates and enhancements.

You may also like

- [On the origin of perpendicular magnetic anisotropy in strained Fe–Co\(–X\) films](#)
L Reichel, A Edström, D Pohl *et al.*
- [Operando Observation of Cobalt Catalysts for Oxygen Evolution By Electrochemical XAFS Technique Using Soft X-Ray](#)
Yosuke Mitsutomi, Masaaki Yoshida, Masanari Nagasaka *et al.*
- [The Annealing Effect on the Magnetic Properties of Fe–Co–B Alloy Films](#)
Y.H. Ghang, S.W. Yung, T.S. Chin *et al.*

From soft to hard magnetic Fe–Co–B by spontaneous strain: a combined first principles and thin film study

L Reichel^{1,2}, L Schultz^{1,2}, D Pohl¹, S Oswald¹, S Fähler¹, M Werwiński^{3,4},
A Edström³, E K Delczeg-Czirjak³ and J Rusz³

¹ IFW Dresden, 01171 Dresden, Germany

² Faculty of Mechanical Engineering, Institute of Materials Science, TU Dresden, 01062 Dresden, Germany

³ Division of Materials Theory, Department of Physics and Astronomy, Uppsala University, SE-751 20, Uppsala, Sweden

⁴ Institute of Molecular Physics, Polish Academy of Sciences, 60-179 Poznań, Poland

E-mail: l.reichel@ifw-dresden.de

Received 3 August 2015, revised 18 September 2015

Accepted for publication 1 October 2015


Published 9 November 2015



Abstract

In order to convert the well-known Fe–Co–B alloy from a soft to a hard magnet, we propose tetragonal strain by interstitial boron. Density functional theory reveals that when B atoms occupy octahedral interstitial sites, the bcc Fe–Co lattice is strained spontaneously. Such highly distorted Fe–Co is predicted to reach a strong magnetocrystalline anisotropy which may compete with shape anisotropy. To probe this theoretical suggestion experimentally, epitaxial films are examined. A spontaneous strain up to 5% lattice distortion is obtained for B content up to 4 at%, which leads to uniaxial anisotropy constants exceeding 0.5 MJ m^{-3} . However, a further addition of B results in a partial amorphisation, which degrades both anisotropy and magnetisation.

Keywords: Fe–Co, rare-earth free permanent magnet, magnetocrystalline anisotropy, tetragonal strain, DFT

 Online supplementary data available from stacks.iop.org/JPhysCM/27/476002/mmedia

(Some figures may appear in colour only in the online journal)

1. Introduction

Fe–Co exhibits one of the highest magnetisations among all magnetic materials [1, 2] and is thus very attractive for applications [3]. Fe–Co–B alloys are well known as soft magnetic materials due to the glass-forming ability of boron [4–7]. In such amorphous materials the magnetocrystalline anisotropy is suppressed. In this study, we demonstrate that Fe–Co–B is also a promising hard magnetic material, when the amorphisation is avoided and the B atoms induce a spontaneous strain in the crystalline lattice.

Within this introduction, we will first summarise criteria for soft and hard magnetic properties. We then use density

functional theory (DFT) to show that introducing B on interstitial sites in the Fe–Co lattice results in spontaneously strained phases with substantial magnetocrystalline anisotropy (MCA). In order to probe the limits of this approach experimentally, we study a series of epitaxial thin films. Results are discussed with respect to the concepts of epitaxial and spontaneous strain in Fe–Co for obtaining rare-earth free permanent magnets. In particular, we relate Fe–Co–B presented here to recently published Fe–Co–C films [8].

Since both, soft and hard magnets require a high magnetisation, Fe–Co [1, 2] is the focus of research. For soft magnetic materials, the magnetic anisotropy should be as low as possible, which is commonly achieved by reducing the grain

size towards nanocrystalline or even amorphous materials [5, 7, 9]. Aiming at hard magnetic properties, a crystalline structure is essential as a magnetocrystalline anisotropy can favour particular directions of magnetisation. The bcc crystal structure of binary Fe–Co, however, exhibits only a low cubic anisotropy [10]. Reducing the crystal symmetry by uniaxial strain is a route to achieve high magnetocrystalline anisotropy in Fe–Co as proposed in different theoretical studies [11–14]. According to these studies, tetragonally strained Fe–Co is considered a possible rare-earth free permanent magnet material. Due to its high magnetostriction [15, 16], Fe–Co indeed appears to be more susceptible to strain compared to e.g. Fe–Ni, which makes Fe–Co less favourable regarding soft magnet applications. Though inverse magnetostriction only describes the influence of low strains, it allows speculation that large strains are beneficial for a high magnetocrystalline anisotropy.

The tetragonal strain is commonly described by the lattice parameters of the strained axis c and the compressed axes a , perpendicular to c . There are two main routes to strain the Fe–Co lattice experimentally. First, in coherent epitaxial growth, Fe–Co thin films adapt the in-plane lattice parameter a from the substrate, which results in an induced strain ($c/a > 1$) due to compressive stress within the film's plane. However, the driving forces for strain relaxation are too high to maintain tetragonal distortion in films thicker than 15 monolayers [17–21], which is equivalent to 2 nm. *In situ* studies [8] revealed that binary Fe–Co films of 4 nm thickness are again cubic with $c/a = 1$. In order to stabilise the strain, calculations based on density functional theory (DFT) [22] motivated an introduction of C atoms on interstitial sites in Fe–Co. Delczeg-czirjak *et al* [22] proposed that about 6 at% of these small atoms establish a c/a ratio of 1.12. In experiments, however, the solubility on interstitial sites is much more limited. Using non-equilibrium preparation methods like pulsed laser deposition (PLD), the limit of solubility, which is only about 0.1 at% for C or B in bcc Fe–Co in thermal equilibrium [24], can be shifted to significantly higher values. PLD prepared Fe–Co films containing 2 at% C exhibit such spontaneous strain with $c/a = 1.03$ up to at least 100 nm thickness as shown in our previous study [8]. In contrast to the induced tetragonal strain at a coherent epitaxial interface, interstitials can result in a minimum of total energy at a certain lattice distortion. This second approach is thus not limited to ultrathin films and accordingly, the strain is also present in thicker films. In analogy to martensitic transformations, we assign this distortion as spontaneous strain, though a direct examination of an associated transformation is difficult, as common DFT only gives the ground state and in thin films, a transformation is often hindered by the rigid substrate [23]. Nevertheless, the energy differences calculated between cubic and tetragonal state are within a factor of two comparable to thermal energies at room temperature and thus transformations are expected to occur in bulk materials.

Computational modeling can act as a powerful guide to experimental studies. Hence, we begin our work by utilising a combination of the most relevant and highly accurate, spin-polarised DFT methods. In the first step, structural properties are modeled with low dopant concentrations being reproduced

by using large supercells and alloying treated in the coherent potential approximation (CPA). The result of these structural studies are then used as input for the next step, where magnetic properties, including magnetic moments of both Fe and Co atoms on each inequivalent site, as well as MAE and orbital moments, are evaluated in fully relativistic calculations including the effect of the crucial spin–orbit coupling.

In PLD, ions with high kinetic energy around 100 eV are deposited [25]. Thus, besides regular deposition, an implantation of the material within the topmost film monolayer takes place [26] and allows for a supersaturation of Fe–Co films with C or B. However, this high energy impact also supports the formation of lattice defects. Supersaturated PLD prepared Fe–Co films with 2 at% C retain c/a ratios of 1.03 up to high film thicknesses [8]. In such spontaneously strained Fe–Co–C, magnetocrystalline anisotropy energies (MAE) of about 0.4 MJ m^{-3} were observed independently from film thickness. Fe–Co with spontaneous strain should not have limitations in film thickness and is thus considered more promising than Fe–Co films with induced strain.

An open question, though, is how the spontaneous strain and the MCA may be further increased. Since the solubility of C in Fe–Co is limited also in PLD prepared films [8], we focus on boron as an atom of comparable size. The location of B in bcc Fe (and similar in bcc Fe–Co) is still under debate. Boron can substitute Fe in the ideal bcc positions [27–29], can occupy interstitial positions [30–33], and B solution in Fe can be stabilised by Ni, N and C [34, 35] both, interstitially and substitutionally [36]. In a more recent theoretical investigation [37], it was shown that B prefers the substitutional chemical disorder in bulk Fe–B. However, this work did not take a local relaxation of the strain around interstitial B atoms into account. The authors further found that surfaces stabilise the occupation of octahedral interstitials. Near free surfaces, the geometrical pressure on B interstitials relaxes. Occupation of octahedral interstitials is followed by an increase of the B–Fe distances and thus a distortion of the bcc lattice. Baik *et al* [37] thus give the motivation to further study the straining effect of B interstitials in Fe(–Co) thin films which are also dominated by free surfaces.

Considering the different interstitial sites in a bcc lattice, a tetragonal strain is exclusively expected, when the B atoms occupy octahedral interstitials. Substitutional arrangements or occupation of tetrahedral interstitials would not change c/a , but only affect the unit cell volume. Octahedral interstitials as defined in [38] exist along all three spatial directions (see supplementary⁵). There are six octahedral interstitial sites in a bcc lattice, indicating a high theoretical solubility, when the atomic radius of the interstitial atom is sufficiently low and chemical conditions are beneficial. If such an interstitial site is occupied by a small atom like B, the atoms of the apexes of the octahedron displace along its axis, i.e. uniaxially. A lattice strain by means of $c/a > 1$ is thus only possible when the octahedral interstitials along the c axis as e.g. (0;0;1/2) within the bcc unit cell are preferentially occupied. The question of how an additional occupation of the other octahedral institials

⁵ See supplementary material at stacks.iop.org/JPhysCM/27/476002/mmedia.

affects the structural properties and the total energy will be discussed based on DFT calculations.

Besides the discussed lattice preferences of boron, amorphisation of the Fe–Co lattice is expected to begin at a certain B content. Depending on the film preparation conditions, amorphous Fe–Co–B phases were reported at B concentrations of e.g. 7.5 [6], 15 [7] or 22 at% [5]. In order to establish a high magnetocrystalline anisotropy in Fe–Co–B, amorphisation has to be avoided. Our study thus presents theoretical calculations of the preference of B atoms to occupy the same type of octahedral interstitials due to lower energy of such configuration. Then it focuses on the MCA evaluation of ideal Fe–Co–B crystals assuming all B impurities occupying the octahedral interstitials perpendicular to the substrate. We then introduce the properties of PLD prepared epitaxial Fe–Co–B films, taking the different possibilities how B may affect the Fe–Co lattice into consideration.

2. Methods

2.1. Computational methods

First principles electronic structure calculations within the generalised gradient approximation (GGA) [39] were used to identify stable or metastable body centered tetragonal (bct) structures for B doped Fe–Co alloys.

In the first step, different B concentrations were modeled by three Fe_yB supercells, Fe_8B , Fe_{16}B and Fe_{24}B with $1 \times 2 \times 2$, $2 \times 2 \times 2$ and $2 \times 2 \times 3$ supercells, respectively. Fe atoms occupy the ideal bcc positions, while B atoms are placed in the octahedral positions, which are the most stable interstitial positions [37]. B dopants in the octahedral positions reproduce the upper limit for tetragonal distortion. Substitutional B dopants were not considered as they do not contribute to the formation of distortion. The conjugate-gradient algorithm as implemented in the Vienna Ab Initio Simulation Package (VASP) [40–43] was used to fully relax these structures. The \mathbf{k} -point mesh was set to $16 \times 16 \times 8$, $8 \times 8 \times 8$, $8 \times 8 \times 6$ for Fe_8B , Fe_{16}B and Fe_{24}B , respectively, within the Monkhorst–Pack scheme [44]. The plane-wave cut off and the energy convergence criterion of the scalar relativistic calculations were set to 500 eV and 10^{-7} eV, respectively.

In the second step, the alloying effect on the equilibrium parameters $(c/a)_{\text{eq}}$ -ratio and volume V_{eq} of these relaxed structures was studied using the exact muffin-tin orbitals—full charge density (EMTO-FCD) method [45–52]. The accuracy of the EMTO method is controlled by the optimised overlapping muffin-tin potential [48, 50, 53]. The muffin-tin potential optimisation procedure is described in detail in [54]. The potential parameter η was chosen to match the equilibrium parameters obtained by EMTO to those obtained by the VASP calculations. The potential parameter η is 0.75, 0.85 and 0.9 for Fe_8B , Fe_{16}B and Fe_{24}B , respectively. The chemical disorder for $(\text{Fe}_{1-x}\text{Co}_x)_y\text{B}$ alloys was treated via the coherent potential approximation (CPA) [55, 56]. The one-electron equations were solved within the scalar-relativistic and soft-core approximations. The Green's functions were calculated for 18 complex energy points distributed exponentially on a semi-circular contour with radius of 1.2 Ry. The 3d and 4s

states of Fe, Co, and the 2s and 2p states of B were treated as valence electrons. s , p , d , f orbitals were included in the muffin-tin basis set ($l_{\text{max}} = 3$). The one-centre expansion of the full-charge density was truncated at $l_{\text{max}}^h = 8$. Between 40 and 500 uniformly distributed \mathbf{k} -points were used in the irreducible wedge of the Brillouin zone. The electrostatic correction to the single-site CPA was described using the screened impurity model [57, 58] with a screening parameter of 0.6. Other screening parameters [59] have been tested for the smallest system and it turned out that their effect on the equilibrium parameters is less than 1%.

The magnetic properties, including magnetic moments and the magnetocrystalline anisotropy energy (MAE), of the various $(\text{Fe}_{1-x}\text{Co}_x)_y\text{B}$ systems were evaluated using the spin-polarised relativistic KKR (SPR-KKR) [60, 61] method in the atomic spheres approximation (ASA), in a similar manner as was done in [22]. Calculations were performed using GGA [39] for the exchange-correlation potential and at least several thousand \mathbf{k} -points (depending on system size) were used for numerical integration over the Brillouin zone in order to obtain well converged values of MAE. Alloying was treated with the CPA [55] and the MAE was obtained by total energy difference for two different magnetisation directions, i.e. $\text{MAE} = E_{\text{total}}(\hat{m}||100) - E_{\text{total}}(\hat{m}||001)$.

All structures from section 3.2 were fully relaxed, c/a ratios and volumes were optimised together with atomic relaxation for every c/a ratio and volume. Those calculations were performed with the full potential linearised augmented plane wave method (FP-LAPW) implemented in the WIEN2k code [62]. For the exchange-correlation potential the GGA form [39] was used. Calculations were performed with a plane wave cut-off parameter $RK_{\text{max}} = 6.5$, total energy convergence criterion 10^{-6} Ry, with $4 \times 4 \times 4$ \mathbf{k} -points and with radii of the atomic spheres 1.96 a_0 for Fe/FeCo and 1.45 a_0 for B, where a_0 is the Bohr radius. The virtual crystal approximation (VCA) was used to study different $\text{Fe}_{0.4}\text{Co}_{0.6}\text{B}$ compositions, following the same procedure as described in [22]. All parameters were carefully tested to provide well converged values.

2.2. Experimental

The Fe–Co–B samples were prepared as thin films performing pulsed laser deposition (PLD) in ultra-high vacuum (5×10^{-9} mbar) at room temperature. The used KrF excimer laser (Coherent LPXpro 305) operates with a wave length of 248 nm and a pulse length of 25 ns. On $\text{MgO}(1\ 0\ 0)$ single crystal substrates, 3 nm Cr seed layers and 30 nm $\text{Au}_{0.55}\text{Cu}_{0.45}$ buffer layers were deposited prior to the deposition of the 20 nm thick Fe–Co–B films. The Au–Cu and the Fe–Co–B layers were prepared in pseudo-co-deposition, i.e. by repetitive changing of the targets during PLD to achieve the aimed compositions. Elemental (Au, Cu, Fe and Co) and a FeB composite target were used therefore. The deposition rates were measured prior the preparation with a quartz crystal rate monitor.

Energy dispersive x-ray spectroscopy (EDX) measurements on a Bruker EDX in a JEOL JSM6510-NX electron microscope confirmed the intended film compositions. The

boron content in the Fe–Co–B films was measured exploiting Auger electron spectroscopy (AES) on a JEOL JAMP-9500F field emission auger microprobe device. The atomic concentrations⁶ were calculated using standard single element sensitivity factors from mean values of sputter depth profiles measurements carried out with 1 keV Ar⁺ ions. Atomic force microscopy (AFM) measurements on an Asylum Research Cypher AFM were performed to study the surface morphologies and to confirm a high flatness of the film surfaces. A Bruker D8 Advance diffractometer operating with CoK α radiation was used for x-ray diffraction (XRD) in Bragg–Brentano geometry. The Fe–Co–B lattice strains were derived from pole figure measurements, which had been carried out on an X’pert four circle goniometer (CuK α radiation). Transmission electron microscopy (TEM) studies were performed on a Titan³ 80–300 microscope, which was equipped with a C_S corrector and a Schottky field emission electron source. The lamella was cut using a focused ion beam on a FEI microscope (Helios NanoLab 600i). For magnetic hysteresis measurements at 300 K, a vibrational sample magnetometer (VSM) mounted in a quantum design physical property measurement system was used.

3. Results and discussion of DFT studies

3.1. Structure optimisation

In order to prepare crystal structures of chemically disordered (Fe_xCo_{1-x})_yB, the simpler Fe_yB systems have to be considered as an initial step. Fe_yB structures are modeled with B atoms placed into octahedral interstitial positions along the *c* axis. This configuration determines the upper limit of the tetragonal distortion. Internal relaxation of Fe atoms around the B interstitials leads to the elongation of *c* and shrinking of *a* lattice parameter. In other words, the *c/a* ratio is now higher than 1, where 1 corresponds to a cubic lattice. The total energies *E* as a function of *c/a* ratio and volume *V* for three Fe_yB systems are computed by VASP and their plots are presented in figure 1.

At each *c/a* ratio, the equilibrium volume (*V*_{eq}) is obtained by using a Morse-type equation of state as minimum of *E*(*V*) dependency. Next, the equilibrium ratio (*c/a*)_{eq} is attained by fitting *E*(*V*_{eq}) with a second order polynomial. Results of (*c/a*)_{eq} and *V*_{eq} are listed in table 1. It is observed that both the *c/a* ratio and volume increase with B content, as expected.

Three types of (Fe_xCo_{1-x})_yB supercells corresponding to different B concentrations have been considered, i.e. (Fe_xCo_{1-x})₈B, (Fe_xCo_{1-x})₁₆B and (Fe_xCo_{1-x})₂₄B, see figure 2. Initially, (Fe_xCo_{1-x})₈B and (Fe_xCo_{1-x})₁₆B were taken into account as reasonable crossing points between computational effort and expected experimental B solubility. Preliminary results suggested that higher B concentration gives higher *c/a* ratio and MAE. Unfortunately, neither 11.1 at% B ((Fe_xCo_{1-x})₈B) nor 5.9 at% B ((Fe_xCo_{1-x})₁₆B) could be obtained experimentally, and what was shown instead, maximum B solubility producing

maximum tetragonal strain is about 4 at%. At that point of this study the (Fe_xCo_{1-x})₂₄B structures (4 at% B) were introduced and calculated.

The effect of substituting Fe by Co on the structural parameters of Fe_yB has been taken into account by using the CPA approximation implemented in the EMTO method. The equilibrium ratios (*c/a*)_{eq} and the lattice parameter *a*_{eq} have been evaluated for the rigid supercells taken from the preceding VASP calculations. Thus, it is important to assess the accuracy of the EMTO method compared to VASP for the pure Fe_yB. For each *c/a* ratio, a fully relaxed structure is generated by VASP at *V*_{eq} and used as input for the EMTO. Total energies are then calculated for each *c/a* ratio and five different *V* while keeping the internal parameters fixed. Results obtained by EMTO, using the above-mentioned fitting procedure for VASP, are listed in table 1. The error bar of the (*c/a*)_{eq} ratio is defined by $\Delta = (c/a)_{eq}^{VASP} - (c/a)_{eq}^{EMTO}$, with *c/a* ratios obtained by VASP and EMTO. Good agreement between these two theoretical methods, regarding both (*c/a*)_{eq} and *V*_{eq}, is observed.

After validation of the EMTO method, the desired CPA structures of (Fe_xCo_{1-x})_yB were evaluated. Results are presented in table 2. It is observed that an increase of Co concentration in (Fe_xCo_{1-x})_yB enhances the tetragonal distortion (*c/a*)_{eq}. At the same time the *a*_{eq} and *V*_{eq} decrease. The decrease in *V*_{eq} is ascribed to the lower atomic volume of Co compared to Fe.

Note, that the tetragonal distortion predicted for B-doped Fe–Co alloys is larger than for C-doped alloys [22]. This can be understood by the fact that the B atomic radius is bigger than the C atomic radius. By adding 4 at% of B a distortion around 1.05–1.07 should be achieved, while for C-doping it is merely about 1.03–1.04. This comparison suggests that B-doping could be a better way to achieve tetragonally distorted Fe–Co alloys.

Note further, that with B-doping, the tetragonal distortion can be obtained for a broader range of Co concentrations, compared to C-doped counterparts. This suggests a possibility to prepare tetragonal Fe–Co alloys with lower Co content. In order to find out whether this brings any advantages, we discuss their magnetic characteristics in sections 3.3 and 3.4.

3.2. Preferential orientation of octahedral interstitials

For a permanent magnet it is imperative that the easy axis of all unit cells is aligned along one particular direction, in which the magnet will be magnetised. The different orientations of octahedral interstitials [38], which could be occupied by the B atoms, thus have to be considered. Consequences of a random distribution have to be discussed as well. The occupation of tetrahedral sites, which just result in a volume change, are not considered in the following since they are energetically unfavourable. Baik *et al* [37] computed that the energy difference between octahedral and tetrahedral sites amounts to 0.70 eV for a cubic Fe–B supercell, without taking into account an optimisation of lattice parameters. The corresponding energy difference calculated by us is 0.77 eV/(B atom), based on bcc Fe 2 × 2 × 2 supercells (Fe₁₆B) with geometry optimisation. This means that B

⁶ In this study, experimentally determined B contents are given in at%, although the DFT calculations deal with (ideal) supercell structures of (Fe–Co)_yB, where B occupies octahedral interstitial sites.

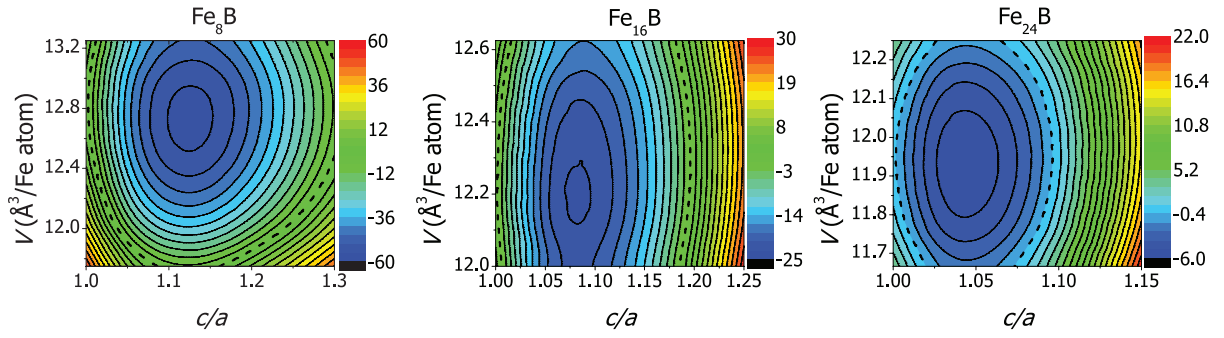


Figure 1. Contour plots of total energy (meV/(Fe atom)) as a function of c/a -ratio and unit volume V , for Fe_8B , Fe_{16}B and Fe_{24}B , respectively. The zero reference values for the energies are $E(c/a = 1, V_{\text{eq}}^{c/a=1})$. The zero energy isolines are denoted by dashed lines. Total energy and volume are normalised per Fe atom.

Table 1. Equilibrium $(c/a)_{\text{eq}}$ ratios and volumes (V_{eq}) of Fe_xB systems obtained by EMT0 and VASP.

Alloy	at% B	$(c/a)_{\text{eq}}$			$V_{\text{eq}}(\text{\AA}^3/(\text{Fe atom}))$	
		VASP	EMT0	Δ	VASP	EMT0
Fe_8B	11.1	1.126	1.132	-0.006	12.73	12.88
Fe_{16}B	5.9	1.089	1.084	0.005	12.21	12.25
Fe_{24}B	4.0	1.050	1.044	0.006	11.93	11.95

atoms favour the octahedral sites even more strongly than Baik *et al* showed. A similar set of calculations for the alloy $(\text{Fe}_{0.4}\text{Co}_{0.6})_{16}\text{B}$, treated within the VCA, gives the energy difference 0.39 eV/(B atom), which also suggests to consider only the octahedral interstitials in the subsequent models.

As our calculations reveal a tetragonal distortion with uniaxial anisotropy along the c axis, independent of the B content, we can take any tetragonal building block for the following considerations, which are borrowed from martensite theory as this can be extrapolated towards the unit cell level [63, 64]. We consider martensite theory as reasonable since the diffusion of B as interstitial [33] is much faster in contrast to Fe (or Co) atoms [66]. In this picture, the orientation of the tetragonal distortion of the Fe–Co ‘martensite’ changes when B moves from one octahedral site to another.

The connection of different tetragonal building blocks is possible by twin boundaries, but they require additional twin boundary energy. A twin boundary is connected with a 90° domain wall in these uniaxial ferromagnets, which further requires magnetic exchange energy. In this simplified picture, both, elastic and magnetic contributions make a different orientation of neighboring tetragonal building blocks energetically unfavourable. Twin boundaries must be introduced, however, to minimise elastic stress energy and magnetostatic energy, and in bulk samples all three orientations are thus equivalent and should occur together.

In order to support this picture on the atomic scale, we performed DFT calculations of a configuration with orthogonal B interstitials and compare it with a uniaxial orientation of B interstitials. For this comparison, one has to consider at least two B atoms per unit cell, whereby the Fe/FeCo supercell has to be enlarged in order to keep low B concentration. In the first step, two Fe based models are considered, both with two B atoms in octahedral interstitial positions in bcc Fe

$3 \times 3 \times 3$ supercells (Fe_{54}B_2), see figure 3. In the orthogonal model (figure 3(a)), the positive strains are generated along two orthogonal axes, which leads to a c/a ratio below 1. In the second model (figure 3(b)), the octahedral interstitial axes are oriented parallel, which forms strain exclusively along the c axis and leads to c/a ratio above 1. Calculations show that the uniaxial configuration is favoured with a difference of total energy equal to 129 meV/(B atom). In order to relate the theoretical result to the experimental Fe–Co–B system one has to go beyond the pure Fe model and, as we did in the previous section, consider the influence of alloying with Co. For this reason, in the second step, the two Fe_{54}B_2 models described above have been recalculated for a selected $\text{Fe}_{0.4}\text{Co}_{0.6}$ concentration within the VCA. Results show once again that the uniaxial configuration is more stable, with slightly lower total energy difference of 126 meV/(B atom). CPA calculations are prohibitively computationally expensive for the EMT0 method due to a large number of inequivalent atoms in the unit cells. Some crystallographic data of the optimised structures are collected in table 3. An interesting result is that the supercell volumes, which for orthogonal and uniaxial configurations were optimised independently, have the same values up to 5 significant digits, which indicates the high accuracy of these results.

With three B atoms per $3 \times 3 \times 3$ bcc Fe supercell it is possible to construct a system with octahedral interstitials in each of the three spatial directions, resulting in a cubic structure. Such a Fe_{54}B_3 structure with a simulated random occupation of the octahedral interstitials, while keeping their mutual distances as large as possible within the supercell, has been carefully optimised together with its uniaxial Fe_{54}B_3 counterpart. The total energy difference between these structures is 49 meV/(B atom) and the preferred configuration of boron is again the uniaxial one. After dividing the latter value by the Boltzmann constant one obtains 570 K/(B atom), the same order of magnitude as room temperature. This implies, that a small fraction of B atoms will occupy positions not yielding a tetragonal strain. Nevertheless, calculations of the presented ideal cases, which may not compare the energies of all theoretical possibilities, but compare the most extreme scenarios, suggest that an occupation of neighboring orthogonal octahedral sites with varying orientation is energetically unfavourable.

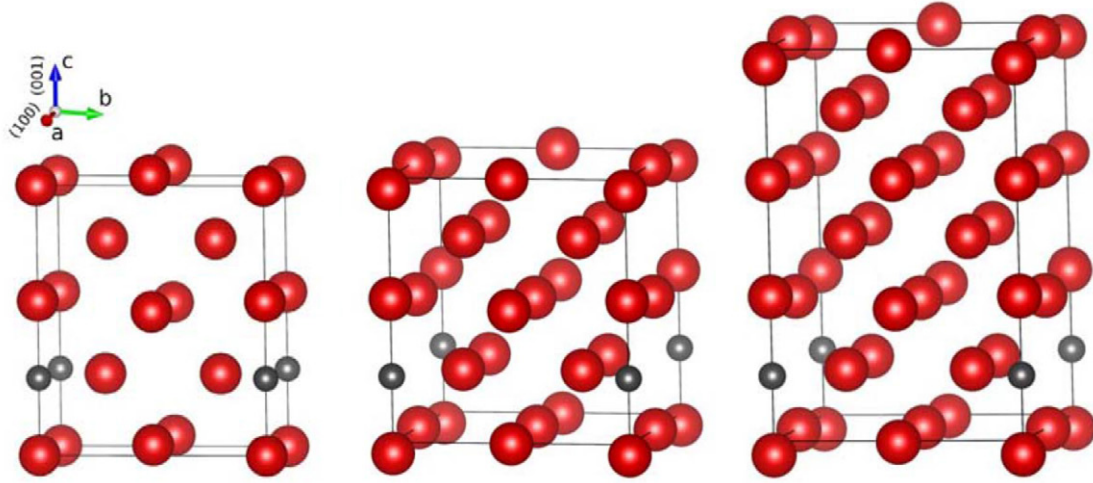


Figure 2. Crystallographic models of $(\text{Fe}_x\text{Co}_{1-x})_8\text{B}$, $(\text{Fe}_x\text{Co}_{1-x})_{16}\text{B}$ and $(\text{Fe}_x\text{Co}_{1-x})_{24}\text{B}$, respectively. The bigger red spheres represent Fe/Co atoms while smaller black spheres denote B atoms.

Table 2. Summary of calculated structural (EMTO) and magnetic (SPR-KKR) characteristics of $(\text{Fe}_x\text{Co}_{1-x})_y\text{B}$ systems.

Composition	$(c/a)_{\text{eq}}$	$a_{\text{eq}} (\text{\AA})$	$V_{\text{eq}} \left(\frac{\text{\AA}^3}{\text{Fe atom}} \right)$	$m_S \left(\frac{\mu_B}{\text{atom}} \right)$	$m_L \left(\frac{\mu_B}{\text{atom}} \right)$	$\mu_0 M_s (\text{T})$	$\text{MAE} \left(\frac{\mu\text{eV}}{\text{atom}} \right)$	$\text{MAE} \left(\frac{\text{MJ}}{\text{m}^3} \right)$
$(\text{Fe}_{0.5}\text{Co}_{0.5})_8\text{B}$	1.247	2.716	12.49	1.71	0.066	1.87	118	1.51
$(\text{Fe}_{0.50}\text{Co}_{0.50})_{16}\text{B}$	1.086	2.809	12.04	1.97	0.068	2.09	46	0.62
$(\text{Fe}_{0.45}\text{Co}_{0.55})_{16}\text{B}$	1.091	2.802	12.00	1.91	0.068	2.04	51	0.69
$(\text{Fe}_{0.40}\text{Co}_{0.60})_{16}\text{B}$	1.103	2.788	11.95	1.86	0.069	2.00	52	0.69
$(\text{Fe}_{0.35}\text{Co}_{0.65})_{16}\text{B}$	1.116	2.774	11.91	1.82	0.069	1.96	43	0.58
$(\text{Fe}_{0.65}\text{Co}_{0.35})_{24}\text{B}$	1.049	2.835	11.95	2.16	0.064	2.26	23	0.31
$(\text{Fe}_{0.60}\text{Co}_{0.40})_{24}\text{B}$	1.051	2.832	11.94	2.12	0.066	2.22	30	0.40
$(\text{Fe}_{0.55}\text{Co}_{0.45})_{24}\text{B}$	1.053	2.827	11.90	2.08	0.067	2.19	30	0.40
$(\text{Fe}_{0.50}\text{Co}_{0.50})_{24}\text{B}$	1.056	2.822	11.87	2.04	0.068	2.15	28	0.38
$(\text{Fe}_{0.45}\text{Co}_{0.55})_{24}\text{B}$	1.059	2.816	11.82	1.99	0.069	2.12	27	0.37
$(\text{Fe}_{0.40}\text{Co}_{0.60})_{24}\text{B}$	1.063	2.810	11.79	1.95	0.070	2.08	29	0.40
$(\text{Fe}_{0.35}\text{Co}_{0.65})_{24}\text{B}$	1.068	2.803	11.76	1.91	0.070	2.04	35	0.48

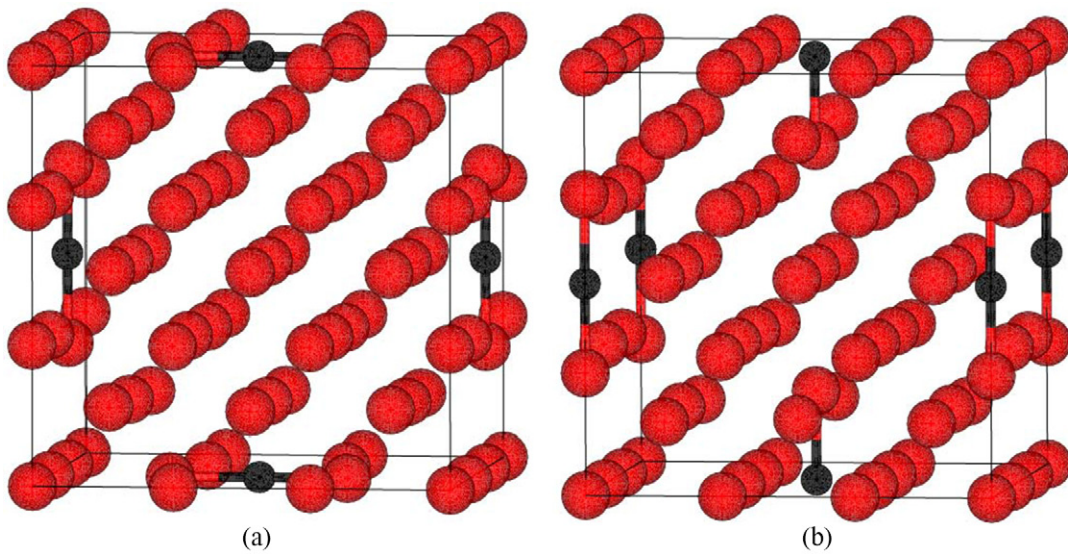


Figure 3. $3 \times 3 \times 3$ bcc Fe supercells with two B atoms in octahedral interstitial positions (Fe_{54}B_2) as (a) orthogonal and (b) uniaxial configuration of interstitial axes. (a) Fe_{54}B_2 orthogonal (b) Fe_{54}B_2 uniaxial.

Table 3. Crystallographic data of optimised Fe_{54}B_2 and $(\text{Fe}_{0.4}\text{Co}_{0.6})_{54}\text{B}_2$ structures and differences of total energies between orthogonal and uniaxial configurations of B interstitials.

	Orthogonal			Uniaxial			$\Delta E \left(\frac{\text{meV}}{\text{B atom}} \right)$
	$V (\text{\AA}^3)$	$a (\text{\AA})$	c/a	$V (\text{\AA}^3)$	$a (\text{\AA})$	c/a	
Fe_{54}B_2	635.74	8.652	0.982	635.74	8.492	1.038	129
$(\text{Fe}_{0.4}\text{Co}_{0.6})_{54}\text{B}_2$	625.31	8.636	0.971	625.31	8.454	1.035	126

From an experimental point of view, the preferential site occupation is tedious to measure directly due to the much lower atomic number of B compared to Fe–Co. However, the reduced symmetry of thin films compared to bulk may result in a favourable orientation, which could be induced by coherent epitaxial growth, followed by a relaxation towards the spontaneously strained state as shown for Fe–Co–C films [8]. A preferential lattice orientation allows using integral methods like texture measurements to probe the present tetragonal distortion and magnetisation measurements to determine the magnetocrystalline anisotropy. An agreement of these global measurements with the local DFT calculations would also confirm the unique alignment of all easy axes, which is beneficial for permanent magnet applications.

In other words, when comparing DFT calculations with experiments, one has to consider the different length scales. In DFT calculations, the preferential c axis is the result of the spontaneous strain at the atomic scale, while in thin film experiments, the out-of-plane orientation is given and may act on the whole sample. The expected preferential alignment of the strained c axis along the out-of-plane orientation thus has to be probed by the following experiments.

3.3. Saturation magnetisation

For the considered $(\text{Fe}_x\text{Co}_{1-x})_y\text{B}$ systems, the influence of B on magnetic moments is regarded first. The average magnetic moments per atom, obtained by SPR-KKR calculations, are listed in table 2. It is observed that the average magnetic moment decreases by increasing the B content. This can be simply explained by addition of a non-magnetic B component itself, and furthermore by the reduction of the magnetic moments on Fe/Co atoms around the B interstitial. In order to look closer at the latter effect an insight into atom and site specific magnetic moments is necessary. Internal relaxation changes the distances between Fe/Co atoms, especially around B interstitials. These reconfigurations affect the exchange coupling between Fe/Co atoms and thus affects magnetic moments.

In table 4 the local magnetic moments for selected $(\text{Fe}_{0.5}\text{Co}_{0.5})_y\text{B}$ systems are presented. The Fe/Co atoms that are the closest neighbours to the B atoms have the magnetic moments most reduced compared to the moments on Fe/Co atoms far from B. The latter values alter rarely, indicating that the Fe/Co atoms far from B have bulk-like characteristics already for $(\text{Fe}_{0.5}\text{Co}_{0.5})_8\text{B}$. This suggests that the influence of a B impurity is relatively short-ranged.

An increase of Co content leads to a decrease of the total magnetic moment for the considered Co concentrations in the

Table 4. Magnetic moments of $(\text{Fe}_{0.5}\text{Co}_{0.5})_y\text{B}$ systems ($\mu_{\text{B}}/\text{atom}$) obtained by SPR-KKR.

Alloy	at% B	Close to B		Far from B	
		m_{Fe}	m_{Co}	m_{Fe}	m_{Co}
$(\text{Fe}_{0.5}\text{Co}_{0.5})_8\text{B}$	11.1	1.74	0.98	2.89	1.95
$(\text{Fe}_{0.5}\text{Co}_{0.5})_{16}\text{B}$	5.9	1.52	0.82	2.85	1.93
$(\text{Fe}_{0.5}\text{Co}_{0.5})_{24}\text{B}$	4.0	1.52	0.85	2.76	1.91

Note: Moments on Fe and Co atoms in the nearest neighbourhood of B octahedral interstitial and as far as possible from B.

$(\text{Fe}_x\text{Co}_{1-x})_{24}\text{B}$ system (see table 2). This negative dependence is not necessarily true beyond the studied range, since for bcc Fe/Co alloys a magnetisation maximum is observed for lower Co concentrations [1, 2]. In our case the drop of magnetic moment is accompanied by an increase of $(c/a)_{\text{eq}}$.

3.4. Magnetocrystalline anisotropy energy

Table 2 summarises the MAEs of the $(\text{Fe}_x\text{Co}_{1-x})_y\text{B}$ systems, as obtained by SPR-KKR calculations. Trends are in many aspects similar as those obtained for interstitial carbon [22]. In particular, the tetragonal distortion of the crystal structure leads to significant values of the MAE under particular c/a and alloy concentrations. Here, however, the reduction in MAE is rather small when going from $y = 16$ to $y = 24$, most likely—as pointed out above—because the c/a values are larger for $y = 24$ with B than with C, which leads to larger MAEs compared to similar dopant concentrations of C. Considering the MAE as a function of Fe concentration x for the case of $y = 24$, there is a rather flat behaviour, but a maximum value of 0.48 MJ m^{-3} is obtained for $x = 0.35$. For $y = 24$ and $x = 0.40$ we obtain $\text{MAE} = 0.40 \text{ MJ m}^{-3}$, which can be compared to $\text{MAE} = 0.19 \text{ MJ m}^{-3}$ obtained with C-doping instead of B. This means that a rather small amount of interstitial B dopants appears to be enough to yield a significant MAE which is promising in a permanent magnet context.

For systems with $y = 24$, we have performed test calculations (not shown) utilising a simpler approach to the problem of alloying, the virtual crystal approximation (VCA), following the same procedure as described in [22]. Although these calculations overestimate the MAE by a factor between 2 and 4 compared to CPA calculations, nevertheless they result in a similar trend and thus provide a further support to the finding that a substantial MAE can be obtained also for lower Co contents. In contrast to CPA results, VCA ones were obtained within a full potential method.

The MAE results can be compared to magnetic semi-hard $(\text{Fe}_x\text{Co}_{1-x})_2\text{B}$ borides [67, 68]. While the latter show a strong

variation of MAE in dependence of the Fe content x , where the MAE can adapt values below and above zero, our results of metallic Fe–Co alloys with much lower B content give MAE well above zero for all studied x .

4. Experimental results and discussion

4.1. Structural properties of Fe–Co–B films

Using PLD, we prepared a boron composition series and studied the structural and magnetic properties of Fe–Co–B films with 20 nm thickness. All films were deposited on $\text{Au}_{0.55}\text{Cu}_{0.45}$ buffer layers, which provide a reduced in-plane lattice parameter compared to Fe–Co and thus induce a c axis oriented film growth [65, 69]. Based on the theoretical results, where the Fe to Co ratio was varied, a composition close to $\text{Fe}_{0.4}\text{Co}_{0.6}$ was chosen as base for our experimental investigations. For the films of this $(\text{Fe}_x\text{Co}_{1-x})\text{--B}$ series, EDX measurements gave $x = 0.38 \pm 0.02$. Corresponding XRD patterns are shown in figure 4(a). The (0 0 2) reflection is the only intensity originating from the Fe–Co–B films and indicates an epitaxial film growth of Fe–Co–B on Au–Cu. No additional phases as e.g. borides, are detected. Pole figure measurements (see the online supplementary data at stacks.iop.org/JPhysCM/27/476002/mmedia) confirm the epitaxial growth without formation of twins. Compared to the position of the $\text{Fe}_{0.38}\text{Co}_{0.62}$ (0 0 2) reflection given in literature [70], we observe a shift to lower 2θ angles for all samples. This indicates already an expanded c axis of the Fe–Co–B lattice, which will be discussed later in detail.

The AES depth profiles, which were carried out to determine the B content of the Fe–Co films, did not reveal a significant variation of the B content in dependence on the sputter depth. This allowed us to determine error bars of the B content for each considered film from its statistical variation. With increasing B content, both a reduced scattering intensity and a peak broadening of the Fe–Co–B(0 0 2) reflection is detected. Applying Scherrer's formula, we estimate the x-ray coherence length of the Fe–Co–B films, which can be taken as measure for the Fe–Co–B crystal size. The results are plotted in figure 4(b). An increase in B content leads to a substantial decrease of coherence length from almost 10 nm in binary $\text{Fe}_{0.38}\text{Co}_{0.62}$ to about 3 nm for the film with 9.6 at% B.

A TEM study of a Fe–Co–B film with 4.2 at% B confirms the crystallinity and continuity of the film (figure 5). The Fourier transform (FT) of the Fe–Co–B film (inset) gives a very regular pattern as expected for an epitaxially grown crystal. Minor contrasts within the Fe–Co–B film may indicate the formation of separated grains with a grain size of approx 5 nm. This would be in agreement with the observed x-ray coherence length (figure 4(b)), but may also be linked to thickness variations of the lamella.

The strong reduction of crystal size at higher B contents as indicated by the XRD measurements (figure 4(b)) has been confirmed by an additional TEM investigation of the film with the highest B content (see the online supplementary data at stacks.iop.org/JPhysCM/27/476002/mmedia), which revealed

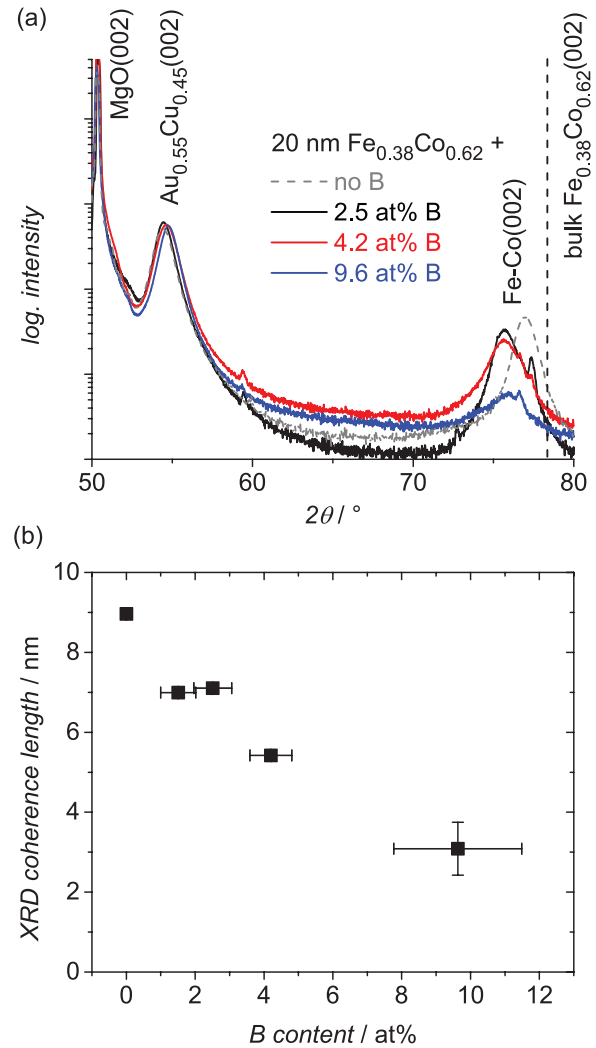


Figure 4. (a) XRD patterns of 20 nm $\text{Fe}_{0.38}\text{Co}_{0.62}\text{--B}$ films with varying B content on $\text{Au}_{0.55}\text{Cu}_{0.45}$ buffers. Relevant reflections are marked. The (0 0 2) equilibrium 2θ angle of binary $\text{Fe}_{0.38}\text{Co}_{0.62}$ is given as broken line. The XRD pattern of a $\text{Fe}_{0.38}\text{Co}_{0.62}$ film without B addition is added for comparison. The intensity maxima near 60° and 77° are attributed to PLD droplets with the composition of the used targets. (b) shows the x-ray coherence length according to Scherrer's formula against the AES determined B content.

oriented nanocrystals of the same diameter surrounded by nanocrystalline and amorphous phases. In the literature, both a formation of Fe–Co–B nanocrystals [9] or amorphous Fe–Co–B [7] are reported for films of similar B contents. Asai *et al* also observed an amorphous structure already at B contents above 5 at% in addition to crystalline Fe–Co–B in $\text{Fe}_{0.7}\text{Co}_{0.3}\text{--B}$ films [7]. Our measurements thus confirm their findings of a decreasing size and fraction of Fe–Co–B crystals with increasing B content in the films. However, all of the presented films contain a significant crystalline fraction which is grown epitaxially. These crystals comprise a certain amount of the alloyed B atoms as is clearly indicated by the change of their lattice parameter c , when compared to the binary $\text{Fe}_{0.38}\text{Co}_{0.62}$ film, which is given as reference in figure 4(a).

In order to characterise the tetragonal strain in the epitaxially grown Fe–Co–B films, {1 0 1} pole figures were measured for all films. As described in [8], the c/a ratios were

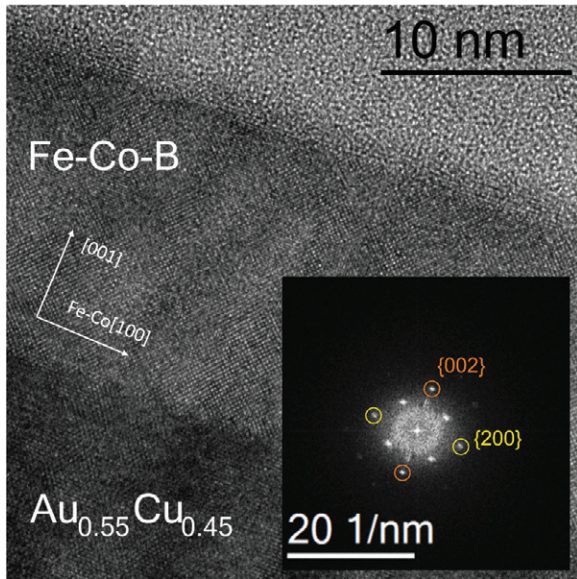


Figure 5. TEM image of a 20 nm $\text{Fe}_{0.38}\text{Co}_{0.62}$ film with 4.2 at% B deposited on $\text{Au}_{0.55}\text{Cu}_{0.45}$. The zone axis is $[0\ 1\ 0]$. The inset shows an FT image of the Fe–Co–B layer. The marked reflections were used for determination of the lattice parameters c and a .

determined from the tilt angles of these planes. In all films, one predominant variant with longer c than in-plane axes was found. No indications for variants with deviating c axis orientation were found. The c/a ratios are plotted in figure 6(a) for the different boron content. An increase of tetragonal distortion is observed with increasing B content up to 4.2 at%. The maximum observed c/a ratio is 1.045 and is achieved for this composition. We can compare this finding to $\text{Fe}_{0.4}\text{Co}_{0.6}$ –C films (open diamonds), which exhibit a maximum tetragonal strain of $c/a = 1.03$ and a lower dependence on the C content as discussed in our previous study [8]. The observation of an increased strain in the Fe–Co–B films qualitatively confirms our theoretical calculations, which predicted an enhanced c/a ratio by about 0.03 in Fe–Co–B when compared to Fe–Co–C. The maximum observed strain with c/a of nearly 1.05 is also reasonably close to the predicted $c/a = 1.063$ for $\text{Fe}_{0.4}\text{Co}_{0.6}$ with 4 at% B (table 2). However, a further increase of B content is not followed by a further increased tetragonal strain, which was predicted by DFT. There are different possible reasons for this difference: (a) The limited solubility of boron in Fe–Co which is nearly zero in thermal equilibrium [24], but is obviously increased substantially by PLD, an effect known for many systems [71]. A limited solubility favours nanocrystalline or amorphous B-rich phases which reduce the effective B content in the Fe–Co matrix and thus also decreases the tetragonal strain. (b) The possible substitutional alloying of B as discussed within the introduction, which would benefit a cubic lattice. And/or (c) the possibility that not all B atoms occupy octahedral interstitials along the axis perpendicular to the film surface, but also interstitials along the in-plane axes are occupied, as e.g. $(1/2;0;0)$ within the bcc unit cell, which benefit a certain in-plane strain, i.e. a reduction of the measured c/a .

All reasons have in common that the amount of B atoms, which contribute in a lattice strain along the c axis, is effectively

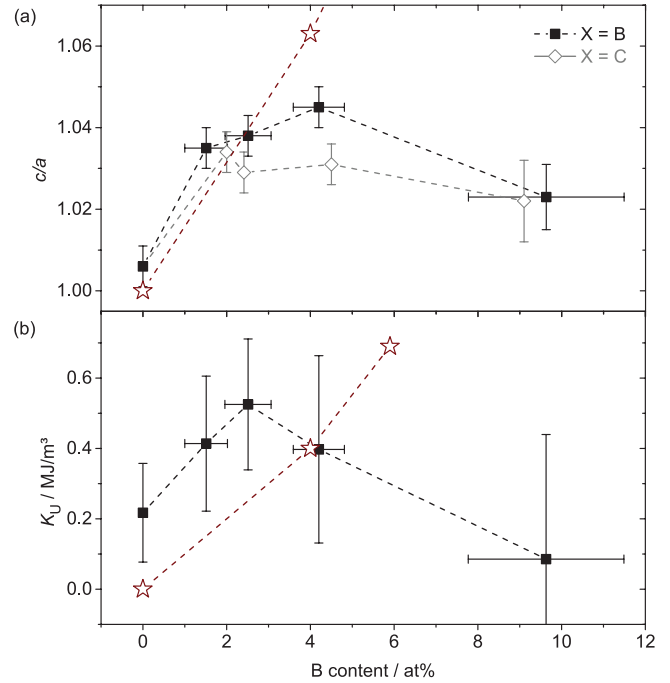


Figure 6. (a) Tetragonal distortion c/a for 20 nm thick $\text{Fe}_{0.38}\text{Co}_{0.62}$ –B films in dependence of the B content (full squares). Results of Fe–Co–C films [8] (open diamonds) have been added for comparison. Note that the film with the highest C content is of Fe–C type and did not contain Co. (b) Corresponding uniaxial magnetic anisotropy constants K_U of the films. The results from the DFT calculations $\text{Fe}_{0.4}\text{Co}_{0.6}$ –B (table 2) have been added as open stars in both graphs. Cubic Fe–Co ($c/a = 1$) with no uniaxial MCA ($K_U = 0$) has been added, although it was not treated in our calculations. Broken lines are guides to the eye.

reduced. Our DFT calculations were based on the assumption that all B atoms occupy octahedral positions along the c axis. As shown in the calculations in section 3.2, the B atoms indeed preferentially align in octahedral interstitials along one particular axis, although all three crystal axes are equivalent in a Fe–Co lattice. The experimental results thus confirm these calculations. However, because of the named reasons, not all B atoms contribute to the c axis oriented strain above a B content of 4.2 at%. A likely explanation why DFT calculations are not able to confirm the experiments exactly is that they do not consider kinetic effects. Films are prepared within a finite time, which may lead to local variations of B density and thus result in an occupation of different lattice sites than expected from DFT, which describes the ground state.

The comparison of the B and C doped Fe–Co films [8] implies that a higher amount of B than C atoms can be solved in the PLD prepared Fe–Co films and preferentially occupies interstitial sites along the c axis, which favours a higher strain. An additional contribution may come from the size of the B atoms, which are bigger than C atoms. However, when a certain limit is reached, further added B (or C) atoms lead to a decrease of c/a . This limit is reached at around 4 at% B (or C). Since the c axis length is not altered when adding more B or C (see figure 4), we conclude that most of the additional atoms occupy sites along the a axes or are dissolved from the Fe–Co crystals. The latter explains the decreasing crystal size with

increasing B (or C) content as discussed in figure 4(b) and in [8], respectively.

For the $\text{Fe}_{0.38}\text{Co}_{0.62}$ film with 4.2 at% B, the lattice distortion was determined from the FT of the TEM images (figure 5). Compared to the XRD result, where c/a was 1.045 (figure 6(a)), we observe a reduced strain of 1.02 ± 0.01 . Such strain reduction after TEM lamella preparation was already reported for Fe–Co–C films and was attributed to a lattice relaxation due to a reduced constraint of a thin TEM lamella compared to a continuous film [8].

From growth studies of Fe–Co–C films, we concluded that the misfit dislocations which form during film growth affect the whole underlying film [69]. Most of the crystal volume is thus expected to exhibit the same strain state. Only a small fraction of the film close to the buffer interface had an increased strain [8], expressed by a c/a ratio increased by 0.02. This also holds for the Fe–Co–B films examined here. The tetragonal strain determined close to the Au–Cu buffer from TEM images of the 4.2 at% B containing $\text{Fe}_{0.38}\text{Co}_{0.62}$ film is 1.05 ± 0.04 . This is about 0.03 higher than the value for the film's volume as determined in TEM, which may be explained by the lower in-plane lattice parameter of $\text{Au}_{0.55}\text{Cu}_{0.45}$ compared to Fe–Co [69]. The TEM studies thus prove that only a very small fraction of the films is influenced by this induced strain at the buffer–film interface and most of the film exhibits a spontaneous strain.

The structural characterisation of the films clearly supports our picture of tetragonally strained Fe–Co–B lattices, where the axis perpendicular to the film surface is preferentially strained and the in-plane axes are compressed. The decisive question of why a predominant amount of B atoms preferentially occupies the octahedral interstitials along this axis, which thus is the strained c axis of the tetragonal lattice (figure 2), may be answered as follows. DFT calculations show that there is a strong energetical preference for two nearby B atoms to occupy the same type of octahedral interstitial position. The substrate may act as a *seed layer* to establish that the first B atoms occupy octahedral interstitial in direction perpendicular to the substrate. The DFT results then suggest that such domain will grow preferentially, compared to a random interstitial occupation or formation of multiple domains, both having higher energy. Multiple variants with differently aligned c axes are unfavourable due to the required interface, i.e. twin boundary, energy. Thus, Fe–Co–B films exhibit a quasi single crystalline state with one preferentially oriented strained c axis. This axis aligns perpendicularly to the film surface due to the square surface symmetry of the Au–Cu buffer.

As second main result, the structural measurements revealed spontaneously strained $\text{Fe}_{0.38}\text{Co}_{0.62}$ –B phases similar to those in Fe–Co–C [8]. The 20 nm thick films are much thicker than coherently strained films. The tetragonal strain is not dependent on film thickness: 100 nm thick films with the same compositions (see the online supplementary data at stacks.iop.org/JPhysCM/27/476002/mmedia) exhibit the same c/a ratios as the films presented here. The studied spontaneously strained Fe–Co–B films confirm our DFT calculations, which suggested minima of total energy depending on

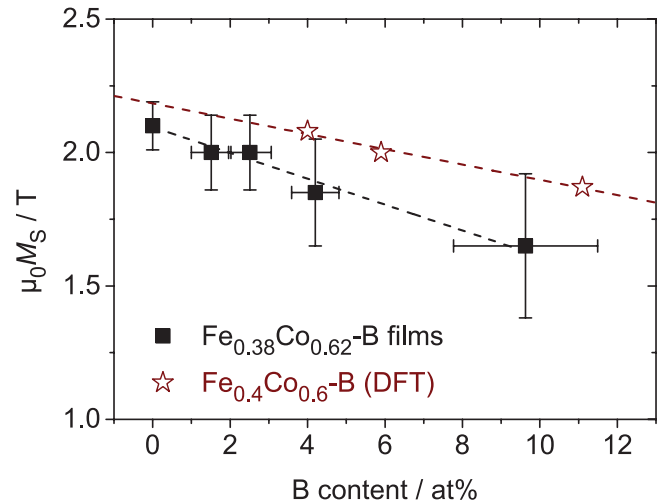


Figure 7. Magnetic saturation $\mu_0 M_S$ in dependence of the B content for the $\text{Fe}_{0.38}\text{Co}_{0.62}$ –B films (squares) and the corresponding calculated structures (stars) according to table 2. Linear fits have been added as broken lines.

the B content (table 2). However, and this is an important difference to the Fe–Co–C films, the spontaneous strain indeed depends on the particular B content—at least for low B content up to about 4 at%.

4.2. Magnetic properties of the $\text{Fe}_{0.38}\text{Co}_{0.62}$ –B films

In order to compare the magnetic properties of spontaneously strained Fe–Co–B films, the anisotropy constant K_U of the strain related uniaxial MCA was determined from hysteresis measurements as described in [8]. The results are summarised in figure 6(b). Similar to c/a , K_U also has a maximum in dependence of the B content. The highest MCA with $K_U = 0.53 \text{ MJ m}^{-3}$ is reached in the 2.5 at% B containing $\text{Fe}_{0.38}\text{Co}_{0.62}$ film. Films with smaller B content have a lower MCA because of their reduced tetragonal strain. B contents above 2.5 at% in $\text{Fe}_{0.38}\text{Co}_{0.62}$ do not increase the MCA, although the c/a ratio's maximum is at a B content of 4.2 at% (figure 6(a)). The observed decrease of MCA with further increased B content occurs simultaneously with a significant reduction of saturation magnetisation in the films (figure 7). While our theoretical results described a reduction of M_S by about 1.5% with each percent B (open stars), the experiments (squares) reveal a stronger dependence between B content and magnetic saturation: The decrease is about 2.5% with each 1 at% B. A possible reason might be a decreased Curie temperature due to the addition of B. However, this is not expected [72] for B additions in Fe. We rather attribute the higher dependence of M_S on the B content to a stronger perturbation of the Fe–Co lattice by the B atoms in the PLD prepared films than is described by the CPA approach, where the B atoms occupy regularly distributed interstitials. The calculations already revealed that Fe and Co atoms have a strongly reduced magnetic moment, when B is their nearest neighbour. In comparison to our experimental study, magnetron sputtered Fe–Co–B films [5], where the material was deposited with substantially lower kinetic

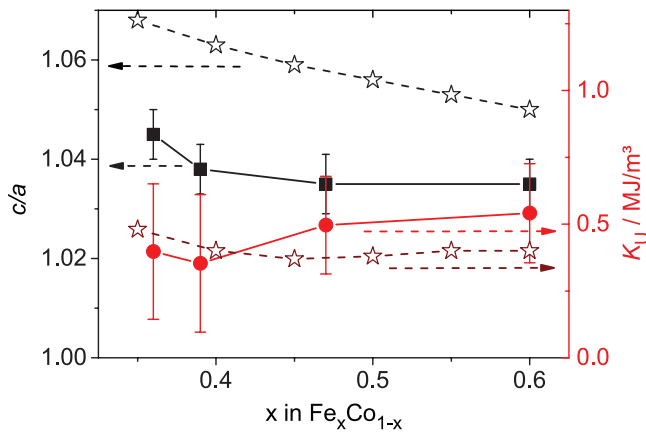


Figure 8. Measured tetragonal lattice strain (full squares) and uniaxial magnetocrystalline anisotropy constants K_U (full circles) in dependence on Fe–Co ratio in 20 nm films with 4 at% B on $\text{Au}_{0.55}\text{Cu}_{0.45}$. DFT results for c/a and K_U are added (open stars).

energy, exhibit a lower decrease of M_S with increasing B content, namely 1.5% per added 1 at% B, which is consistent with our theoretical results (table 2).

We argue that both, the strong reduction of M_S and the decrease of MCA observed in our samples originate from an interplay of the proceeding reduction of crystallinity due to the increasing B content and the high energy impact of the ions during PLD [25] which may disturb the local environment of the Fe and Co atoms drastically. However, when we compare the theoretical and the experimental results of K_U (figure 6(b)), we find increased values for the $\text{Fe}_{0.38}\text{Co}_{0.62}$ –B thin films at low B contents. We attribute this discrepancy to a lack of full potential effects in DFT. At B contents above 4 at%, this underestimation is overcome by the discussed structural effects. We thus observe a very good agreement of the experimentally measured magnetic anisotropy with the theoretically determined value for $(\text{Fe}_{0.4}\text{Co}_{0.6})_{24}\text{B}$, but no longer for $(\text{Fe}_{0.4}\text{Co}_{0.6})_{16}\text{B}$, i.e. 6 at% B (open circles in figure 6(b)).

Concluding the magnetic measurements of the $\text{Fe}_{0.38}\text{Co}_{0.62}$ –B films, we observe a direct dependence of the magnetocrystalline anisotropy on the spontaneous strain for low B contents. However, an increased tetragonality in the Fe–Co–B lattice did not necessarily imply an increased MCA for the complete films due to the formation of nano-crystalline or disturbed regions.

4.3. Structural and magnetic properties in dependence on the Fe/Co ratio

The study of various Fe/Co ratios by DFT calculations (table 2) motivated for a comparison of films with unaltered B content. We chose $\text{Fe}_x\text{Co}_{1-x}$ films with 4 at% B due to the observed strain maximum (figure 6(a)). The measured tetragonal strain and the observed perpendicular anisotropy constants K_U in these 20 nm thick films are summarised in figure 8. With regard to the tetragonal strain, we observe a slight decrease with increasing Fe content. Although there is only little variation between the films, this finding is qualitatively consistent with the theoretical predictions for $(\text{Fe}_x\text{Co}_{1-x})_{24}\text{B}$ in table 2,

which also give higher c/a ratios for higher Co content. For already described reasons, we do not reach as high strains as calculated by DFT. The highest experimentally observed c/a is 1.045 for $x = 0.36$.

When comparing the magnetocrystalline anisotropy energies K_U , we do not observe a strong dependence on the Fe/Co ratio, which in principle fits to the weak dependency proposed by DFT (see figure 8). K_U is about 0.5 MJ m^{-3} on average, but slightly lower on the Co rich side and slightly higher in the films with more Fe than Co. The maximum observed K_U is 0.54 MJ m^{-3} for $x = 0.6$. The DFT calculations, however, predicted the highest MCA for the lowest Fe content.

From the $\text{Fe}_x\text{Co}_{1-x}$ films with 4 at% B we thus conclude that higher Fe content ($x = 0.6$) not only lead to a higher magnetic saturation M_S , but are also beneficial for a high MCA at low tetragonal strain. Such Fe rich films or additional concepts to stabilise higher strains beyond $c/a = 1.05$ obtained here are considered promising for further research. As one way to fulfil the latter task, we suggest the choice of a preparation method with less energetic impact, where the effect of lattice perturbation due to the B atoms might be smaller.

5. Conclusion

In this combined theory-experimental study, Fe–Co–B is introduced as an alloy with spontaneous strain and hard magnetic properties. Structure calculations based on EMTO predict strong tetragonal lattice distortions up to $c/a = 1.25$ in dependence on the B content, if all B atoms occupy octahedral interstitials along the c axis. This arrangement is preferential, when compared to an occupation of other possible interstitial sites. SPR-KKR results for the distorted Fe–Co–B lattices give strong magnetocrystalline anisotropies when the former cubic symmetry is broken. For 11 at% B, K_U should be comparable to shape anisotropy. Experiments, however, show that the amount of B atoms which strains the Fe–Co lattice is limited. At a B content higher than 4 at%, the strain decreases. A supersaturation of the octahedral lattice sites with B atoms is considered to be responsible for this deviation from the ideal behaviour of B interstitials as treated in DFT. For low B contents, our theoretical results are well confirmed by experiments, in particular when regarding K_U . The highest magnetocrystalline anisotropies are observed for $\text{Fe}_{0.38}\text{Co}_{0.62}$ with 2.5 at% B or in Fe richer $\text{Fe}_{0.6}\text{Co}_{0.4}$ with 4 at% B. K_U of these alloys is above 0.5 MJ m^{-3} . Although this value does not exceed the shape anisotropy, the spontaneous strain should allow for a preparation of Fe–Co–B with an easy axis of magnetisation, which is defined by structure and not by shape. The approach to exploit spontaneous strain and the related MCA thus gives much more opportunities than the substrate induced strain in Fe–Co, where the strain is limited to ultrathin films.

Acknowledgments

We acknowledge funding of the EU through FP7-REFREEPERMAG. For TEM lamella preparation, we thank

Christine Damm, Juliane Scheiter and Almut Pöhl. The authors further thank Levente Vitos, Christian Behler and Ruslan Salikhov for discussion. Calculations were performed on UPPMAX, NSC-Matter, Triolith and C3SE resources. E K Delczeg-Czirjak and J Rusz acknowledge the Swedish Research Council for financial support.

References

- [1] Victora R H and Falicov L M 1984 *Phys. Rev. B* **30** 259
- [2] James P, Eriksson O, Johansson B and Abrikosov I A 1999 *Phys. Rev. B* **59** 419
- [3] Coey J M D 2001 *J. Alloys Compd.* **326** 2
- [4] O'Handley R C 1977 *Solid State Commun.* **21** 1119
- [5] Kim I, Kim J, Kim K H and Yamaguchi M 2004 *IEEE Trans. Magn.* **40** 2706
- [6] Yang A, Imrane H, Lou J, Kirkland J, Vittoria C, Sun N and Harris V G 2008 *J. Appl. Phys.* **103** 07E736
- [7] Asai Y, Ohtake M, Kawai T and Futamoto M 2013 *J. Korean Phys. Soc.* **63** 733
- [8] Reichel L et al 2014 *J. Appl. Phys.* **116** 213901
- [9] Minor M K, Crawford T M, Klemmer T J, Peng Y and Laughlin D E 2002 *J. Appl. Phys.* **91** 8453
- [10] Shih J W 1934 *Phys. Rev.* **46** 139
- [11] Burkert T, Nordstr L, Eriksson O and Heinonen O 2004 *Phys. Rev. Lett.* **93** 027203
- [12] Neise C, Schönecker S, Richter M, Koepnik K and Eschrig H 2011 *Phys. Status Solidi B* **248** 2398
- [13] Kota Y and Sakuma A 2012 *Appl. Phys. Express* **5** 113002
- [14] Turek I, Kudrnovsky J and Carva K 2012 *Phys. Rev. B* **86** 174430
- [15] Hall R C 1960 *J. Appl. Phys.* **31** S157
- [16] Pfeifer F and Radeloff C 1980 *J. Magn. Magn. Mater.* **19** 190
- [17] Andersson G, Burkert T, Warnicke P, Björck M, Sanyal B S, Chacon C, Zlotea C, Nordström L, Nordblad P and Eriksson O 2006 *Phys. Rev. Lett.* **96** 037205
- [18] Winkelmann A, Przybylski M, Luo F, Shi Y and Barthel J 2006 *Phys. Rev. Lett.* **96** 257205
- [19] Luo F, Fu X L, Winkelmann A and Przybylski M 2007 *Appl. Phys. Lett.* **91** 262512
- [20] Yildiz F, Luo F, Tieg C, Abrudan R M, Fu X L, Winkelmann A, Przybylski M and Kirschner J 2008 *Phys. Rev. Lett.* **100** 037205
- [21] Yildiz F, Przybylski M, Ma X-D and Kirschner J 2009 *Phys. Rev. B* **80** 064415
- [22] Delczeg-Czirjak E K, Edström A, Werwiński M, Rusz J, Skorodumova N V, Vitos L and Eriksson O 2014 *Phys. Rev. B* **89** 144403
- [23] Buschbeck J, Opahle I, Richter M, Rö U K, Klaer P, Kallmayer M, Elmers H J, Jakob G, Schultz L and Fähler S 2009 *Phys. Rev. Lett.* **103** 216101
- [24] Cameron T B and Morral J E 1986 *Metall. Trans. A* **17** 1481
- [25] Fähler S and Krebs H-U 1996 *Appl. Surf. Sci.* **96–98** 61
- [26] Fähler S, Weisheit M, Kahl S, Sturm K and Krebs H U 1999 *Appl. Phys. A* **69** S459
- [27] Busby P E, Warga M E and Wells C 1953 *J. Met.* **5** 1462
Busby P E and Wells C 1954 *J. Met.* **6** 972
- [28] Shevelev A K 1958 *Dokl. Akad. Nauk SSSR* **123** 453
- [29] Strocchi P M, Melandri B A and Tamba A 1967 *Nuovo Cimento B* **51** 1
- [30] Hasiiguti R R and Kamoshita G 1954 *J. Phys. Soc. Japan* **9** 646
- [31] Thomas W R and Leak G M 1955 *Nature* **176** 29
- [32] Tavadze F N, Bairamashvili I A and Metreveli V S 1965 *Soobshch. Akad. Nauk. Gruz. SSR* **40** 401
- [33] Wang W, Zhang S and He X 1995 *Acta Metall. Mater.* **43** 1693
- [34] Hayashi Y and Sugeno T 1970 *Acta Metall.* **18** 693
- [35] Lucci A and Venturello G 1971 *Scr. Metall.* **5** 17
- [36] Fors D H R and Wahnström G 2008 *Phys. Rev. B* **77** 132102
- [37] Baik S S, Min B I, Kwon S K and Koo Y M 2010 *Phys. Rev. B* **81** 144101
- [38] Leslie W C and Hornbogen E 1996 *Physical Metallurgy* 4th edn, ed R W Cahn and P Haasen (Amsterdam: Elsevier) chapter 17
- [39] Perdew J P, Burke K and Ernzerhof M 1996 *Phys. Rev. Lett.* **77** 3865
- [40] Kresse G and Furthmüller J 1996 *Comput. Mater. Sci.* **6** 15
- [41] Kresse G and Furthmüller J 1996 *Phys. Rev. B* **54** 11169
- [42] Blöchl P E 1994 *Phys. Rev. B* **50** 17953
- [43] Kresse G and Joubert D 1999 *Phys. Rev. B* **59** 1758
- [44] Monkhorst H J and Pack J D 1976 *Phys. Rev. B* **13** 5188
- [45] Andersen O K, Jepsen O and Krier G 1994 *Lectures on Methods of Electronic Structure Calculation* (Singapore: World Scientific) p 63
- [46] Andersen O K, Arcangeli C, Tank R W, Saha-Dasgupta T, Krier G, Jepsen O and Dasgupta I 1998 *Mater. Res. Soc. Symp. Proc.* **491** 3
- [47] Vitos L, Skriver H L, Johansson B and Kollár J 2000 *Comput. Mater. Sci.* **18** 24
- [48] Vitos L 2001 *Phys. Rev. B* **64** 014107
- [49] Vitos L, Abrikosov I A and Johansson B 2001 *Phys. Rev. Lett.* **87** 156401
- [50] Vitos L 2007 *The EMTO method and applications Computational Quantum Mechanics for Materials Engineers* (London: Springer)
- [51] Vitos L, Kollar J and Skriver H L 1997 *Phys. Rev. B* **55** 13521
- [52] Kollár J, Vitos L and Skriver H L 2000 *Electronic Structure and Physical Properties of Solids: the Uses of the LMTO Method (Lectures Notes in Physics)* ed H Dreyssé (Berlin: Springer) p 85
- [53] Zwierzycki M and Andersen O K 2009 *Acta Phys. Pol. A* **115** 64
- [54] Al-Zoubi N, Skorodumova N V, Medvedeva A, Andersson J, Nilson G, Johansson B and Vitos L 2012 *Phys. Rev. B* **85** 014112
- [55] Soven P 1967 *Phys. Rev.* **156** 809
- [56] Györfy B L 1972 *Phys. Rev. B* **5** 2382
- [57] Korzhavyi P A, Ruban A V, Abrikosov I A and Skriver H L 1995 *Phys. Rev. B* **51** 5773
- [58] Ruban A V and Skriver H L 2002 *Phys. Rev. B* **66** 024201
- [59] Rahaman M, Ruban A V, Mookerjee A and Johansson B 2011 *Phys. Rev. B* **83** 054202
- [60] Ebert H, Ködderitzsch D and Minár J 2011 *Rep. Prog. Phys.* **74** 096501
- [61] Ebert H 2012 *The Munich SPR-KKR package, version 6.3* <http://ebert.cup.uni-muenchen.de/SPRKKR>
- [62] Blaha P, Schwarz K, Madsen G, Kvasnicka D and Luitz J 2001 *WIEN2k, An Augmented Plane Wave + Local Orbitals Program for Calculating Crystal Properties* ed K Schwarz (Vienna: Technische Universität Wien)
- [63] Kaufmann S, Rößler U K, Heczko O, Wuttig M, Buschbeck J, Schultz L and Fähler S 2010 *Phys. Rev. Lett.* **104** 145702
- [64] Kauffmann-Weiss S, Gruner M E, Backen A, Schultz L, Entel P and Fähler S 2011 *Phys. Rev. Lett.* **107** 206105

- [65] Kauffmann-Weiss S, Hamann S, Reichel L, Siegel A, Heller R, Schultz L and Fähler S 2014 *APL Mater.* **2** 046107
- [66] Buffington F S, Hirano K and Cohen M 1961 *Acta Metal.* **9** 434
- [67] Kuz'min M D, Skokov K P, Jian H, Radulov I and Gutfleisch O 2014 *J. Phys.: Condens. Matter* **26** 064205
- [68] Belashchenko K D, Ke L, Däne M, Benedict L X, Lamichhane T N, Taufour V, Jesche A, Bud'ko S L, Canfield P C and Antropov V P 2015 *Appl. Phys. Lett.* **106** 062408
- [69] Reichel L, Schultz L and Fähler S 2015 *J. Appl. Phys.* **117** 17C712
- [70] Predel B 1993 Co-Fe (Cobalt-Iron) *SpringerMaterials: the Landolt-Börnstein Database* ed O Madelung (Berlin: Springer)
- [71] Krebs H-U 1997 *J. Non-Equilib. Process.* **10** 3
- [72] Hasegawa R and Ray R 1978 *J. Appl. Phys.* **49** 4174